Spherical Hands: Toward Underactuated, In-Hand Manipulation Invariant to Object Size and Grasp Location

Raymond R. Ma
Department of Mechanical Engineering and Materials Science,
Yale University,
9 Hillhouse Avenue,
New Haven, CT 06511
e-mail: raymond.ma@yale.edu

Nicolas Rojas
Department of Engineering and Design,
School of Engineering and Informatics,
University of Sussex,
Brighton BN1 9QT, UK

Aaron M. Dollar
Department of Mechanical Engineering and Materials Science,
Yale University,
15 Prospect Street,
New Haven, CT 06520
e-mail: aaron.dollar@yale.edu

Minimalist, underactuated hand designs can be modified to produce useful, dexterous, in-hand capabilities without sacrificing their passive adaptability in power grasping. Incorporating insight from studies in parallel mechanisms, we implement and investigate the "spherical hand" morphologies: novel, hand topologies with two fingers configured such that the instantaneous screw axes, describing the displacement of the grasped object, always intersect at the same point relative to the palm. This produces the same instantaneous motion about a common point for any object geometry in a stable grasp. Various rotary fingertip designs are also implemented to help maintain stable contact conditions and minimize slip, in order to prove the feasibility of this design in physical hand implementations. The achievable precision manipulation workspaces of the proposed morphologies are evaluated and compared to prior human manipulation data as well as manipulation results with traditional three-finger hand topologies. Experiments suggest that the spherical hands' design modifications can make the system's passive reconfiguration more easily predictable, providing insight into the expected object workspace while minimizing the dependence on accurate object and contact modeling. We believe that this design can significantly reduce the complexity of planning and executing dexterous manipulation movements in unstructured environments with underactuated hands.
[DOI: 10.1115/1.4034787]

1 Introduction

Past work [1–4] has shown that underactuated hands with carefully selected mechanical design parameters can produce passively adaptive grasps with minimal control and hardware complexity. This has led to simpler and more compact designs while retaining a comparable level of grasping functionality, which is very useful for mobile and service robotics applications in unstructured environments. However, research in underactuated hands' ability to perform precision in-hand manipulation, which remains a difficult task even for complex, redundantly actuated hands, has been limited. Dexterous in-hand manipulation extends the utility of hands to beyond just acquiring and maintaining grasps, allowing for fine adjustments to the position and orientation of the grasped object [5]. This typically requires redundant control schemes with feedback, as well as detailed knowledge of the object geometry and fingertip contact locations, which may be difficult to acquire outside of a controlled and well-calibrated environment. The additional degrees-of-freedom (DOF) that enable adaptive compliance in enveloping grasps make these tasks with underactuated or soft robotics more challenging. In general, the behavior of all soft, deformable, and reconfigurable elements needs to be properly evaluated and modeled for each unique object geometry [6,7].

In this paper, we detail work on the *spherical hands*, design morphologies that build upon a common three-fingered hand structure used in several commercial hands by arranging underactuated fingers with out-of-plane offsets such that their joint axes intersect at a common reference point. These hand morphologies are called spherical hands because the intersecting joint axes of these fingers result in an object workspace where all instantaneous motions are about the same point, regardless of object geometry or points of contact. It has been shown that these proposed modifications can be made without negating the adaptive, power-grasping capability of the original design [8]. Figure 1 shows a physical example of one of these designs, highlighting the common point N about which the object is restricted to move. We also consider the incorporation of specialized, passively rotary fingertips to minimize undesirable slip or rolling conditions at contact, as well as a passive abduction/adduction pivot at the thumb base,

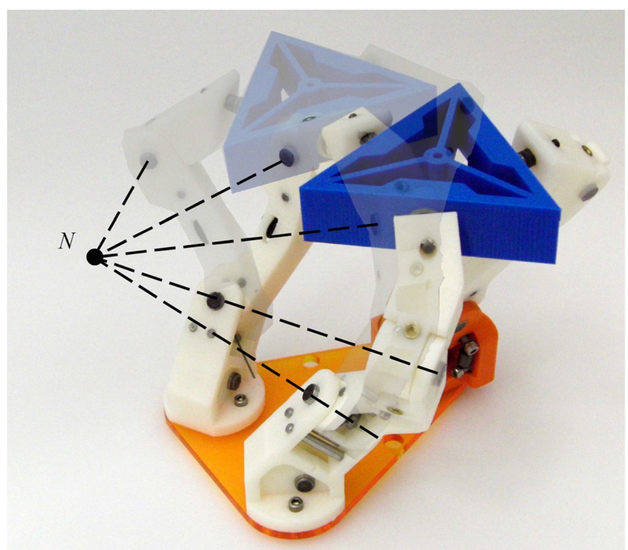

Fig. 1 Spherical hands are hand topologies incorporating curved fingers with out-of-plane angular offsets designed such that the grasped-object motion is about a common point *N*, regardless of contact location or system configuration

Manuscript received March 24, 2016; final manuscript received September 5, 2016; published online October 25, 2016. Assoc. Editor: Leila Notash.

to maximize precision grasp stability over an extended range of object poses.

Other researchers have found inspiration from the parallel mechanisms research domain, identifying closed-chain mechanisms as a useful, albeit idealized, model for precision manipulation with both fully actuated [9] and underactuated [10] hands. In particular, studies in parallel wrist design [11] have suggested optimal design strategies for specific classes of motions. Researchers [12] have established frameworks to describe dexterous in-hand manipulation in the context of parallel mechanisms, assuming the contact conditions remain valid. The spherical hand morphology incorporates insight from these studies on parallel mechanisms to generate object workspaces with the same predictable characteristic regardless of the object geometry and contact locations.

The rest of this paper is organized as follows: In Sec. 2, the theoretical basis for the spherical hand morphologies is presented and shows how the grasped object displacement primarily reduces to a spherical rotation around a fixed point, independent of the object properties or hand configuration. Section 3 describes the mechanical design and fabrication of the spherical hand fingers and the thumb's passive pivot base. The two experimental setups used to evaluate the spherical hand designs are then described: an unactuated setup that uses magnetic spherical joints in place of the fingertip contacts in Sec. 4, and the fully assembled, actuated hand with rotary fingertips in Sec. 5. Finally, the results' implications and comparison to those of traditional and novel modified three-fingered robot hand implementations as well as past work on human manipulation workspaces are discussed in Sec. 6.

2 Spherical Hands

Traditional hand designs typically use fingers with flexion motion primarily constrained to a plane, and many researchers have evaluated mechanical enhancements to the basic hand topology. For example, Dai et al. [1] have investigated the utility of an articulated palm structure based on a spherical five-bar linkage, Higashimori et al. [2] proposed a rotary base to decouple the hand into two independent grasping pairs, and Bicchi and Marigo [3] has presented efforts in attaching actuated, rotary features onto gripper surfaces. Although some designs [4,5] utilize compliant flexure joints or soft materials to enable out-of-plane deflection, no studies, to the authors' knowledge, have investigated the utility of fingers with spatial flexion motion profiles. In this section, we show that by configuring the finger design and attachment such that their revolute axes intersect at a common point, the finite displacement of the corresponding grasped object always reduces to a spherical rotation around that point.

The common point can be calculated from the geometry of the hand alone, independent of the particularities of the grasped object. This property is particularly useful for underactuated hands, as neither the final configuration nor contact locations are always independently controllable. The full hand-object system needs to be considered to determine each stable, precision-grasp pose, and changes in force control usually lead to system reconfiguration. In past work on underactuated precision manipulation [6], the achievable object workspace needed to be experimentally validated by exhaustively sampling the actuation space for each unique object geometry. In contrast, the spherical hand concept establishes an invariant, kinematic characteristic of the object workspace independent of the system's internal forces or pose. This increases performance repeatability and robustness to operational errors.

Figure 2 shows the model of a spherical hand with conventional, two-link, no-pivot (NP) thumb, and two customized opposing fingers, holding a general object—represented as a triangular object in the image—in a precision grasp. The two opposing fingers have joint axes that intersect at a common point in space. We will refer to these two fingers as the *curved fingers* in the interest of brevity.

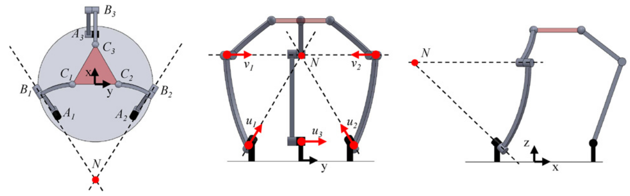

Fig. 2 Multiple views of the kinematic structure of the proposed spherical hand, with a traditional two-link thumb and nonpivoting base. The axes of rotation for the curved fingers intersect at a common point regardless of the hand configuration.

During in-hand manipulation, the hand-object system of this spherical hand is equivalent to a closed kinematic chain composed of eight links with three revolute-revolute-spherical serial limbs that connect the palm of the robot hand, or base, to the grasped object. The spherical joints at the object-hand interface can be assumed to have joint limits reflecting the hand's ability to passively or actively maintain the desired contact constraints, such that the behavior of the hand-object system will be a subset of the ideal kinematic chain model. The mobility of these closed kinematic chains (eight links, nine joints in $\mathbb{E}^3$ with a total number of 15 degrees-of-freedom in the joints) is 3, by applying the Hunt's form of the Chebychev–Grübler–Kutzbach criterion [7]. Consequently, the feasible movements of the grasped object correspond to a three-manifold (embedded in $\mathbb{E}^3$). By operating in the subset of actuation space where the reconfiguration and passive compliant elements in the system can be leveraged to maintain the contact constraints at the object-hand interface, three total actuators (one per finger) should be sufficient to move the object in all three degrees of motion [8].

2.1 Kinematic Reduction.

References [13,14] describe a precision analysis method that determines the composition of the displacement manifold of a grasped object relative to the palm and defines the displacements that can be controlled by the hand actuators without depending on external factors. This approach is based on a reduction of the graph of kinematic constraints related to the hand-object system through proper manipulations of the continuous subgroups of displacements generated by the hand joints and contacts.

According to the notation of Fig. 2, let us call finger 1, finger 2, and finger 3, the fingers with contact points C_1, C_2, and C_3, respectively. Fingers 1 and 2 are the curved fingers, typically the fingers with coupled abduction/adduction base rotations in commercial hands [6,11,12], and finger 3 is the opposition thumb. For finger 1, one of the curved fingers, the axis of the ground revolute joint (or proximal joint) is determined by a unit vector $\boldsymbol{u}_1$ and any point, say A_1, that belongs to the line defined by the rotational axis. Thus, point A_1 can be N, the point where the rotational axes of the curved fingers intersect. This kinematic pair corresponds to a kinematic constraint that forms the subgroup of displacements $\{\mathbf{R}(A_1, \boldsymbol{u}_1)\} = \{\mathbf{R}(N, \boldsymbol{u}_1)\}$ that restrict the movement between this proximal link and the palm. Similarly, for the finger 1's distal joint, the generated subgroup is $\{\mathbf{R}(B_1, \boldsymbol{v}_1)\} = \{\mathbf{R}(N, \boldsymbol{v}_1)\}$. For the case of the motion constraint between the fingertip and the object, the generated subgroup is $\{\mathbf{S}(C_1)\}$, which corresponds to a spherical rotation about point C_1. This contact model is kinematically equivalent to point contact with friction [15]. The same analysis can be repeated for finger 2, the other curved finger.

In the case of finger 3 (thumb), the axis of the ground revolute joint, defined by the unit vector $\boldsymbol{u}_3$ and the point A_3, is parallel to the y -axis. In this finger, the axis of the revolute distal joint is parallel to the axis of the proximal joint. The resulting graph of kinematic constraints for the complete hand-object system of this spherical hand is depicted in Fig. 3(*a*). This graph is composed of

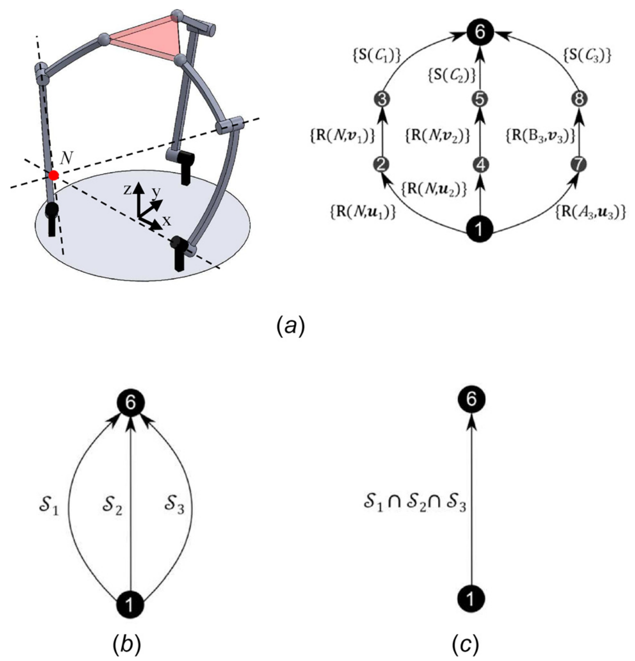

Fig. 3 The graph of kinematic constraints of the hand-object system for the spherical hand (*a*) and its corresponding reduction ((*b*) and (*c*))

eight nodes and nine edges, related to number of links and joints of the associated kinematic chain, respectively.

In order to obtain a mathematical characterization of the displacement manifold of the grasped object relative to the palm of the spherical hand with two-link thumb of static base, that is, to reduce the graph to a graph of two nodes with a single kinematic constraint, we firstly apply, according to the notation of Fig. 3(*a*), a serial reduction to the nodes 1, 2, 3, and 6. Then, we get

$$\mathcal{S}_1 = \{\mathbf{R}(N,\boldsymbol{u}_1)\}\cdot\{\mathbf{R}(N,\boldsymbol{v}_1)\}\cdot\{\mathbf{S}(C_1)\} \tag{1}$$

Using the property of closure of groups, it can be easily proven that $\{\mathbf{S}(O)\} = \{\mathbf{R}(O,\boldsymbol{i})\}\cdot\{\mathbf{R}(O,\boldsymbol{j})\}\cdot\{\mathbf{R}(O,\boldsymbol{k})\}$, provided that $\boldsymbol{i}$, $\boldsymbol{j}$, and $\boldsymbol{k}$ are linearly independent vectors [16]. Let $\widehat{\boldsymbol{nc}_1}$ a unit vector that is parallel to the line defined by points N and C_1, and $\boldsymbol{j}_1$ and $\boldsymbol{k}_1$, two unit vectors that are linearly independent to it. Then

$$\begin{aligned}\{\mathbf{S}(C_1)\} &= \{\mathbf{R}(C_1,\widehat{\boldsymbol{nc}_1})\}\cdot\{\mathbf{R}(C_1,\boldsymbol{j}_1)\}\cdot\{\mathbf{R}(C_1,\boldsymbol{k}_1)\}\\ &= \{\mathbf{R}(N,\widehat{\boldsymbol{nc}_1})\}\cdot\{\mathbf{R}(C_1,\boldsymbol{j}_1)\}\cdot\{\mathbf{R}(C_1,\boldsymbol{k}_1)\}\end{aligned} \tag{2}$$

since $\{\mathbf{R}(C_1,\widehat{\boldsymbol{nc}_1})\} = \{\mathbf{R}(N,\widehat{\boldsymbol{nc}_1})\}$. Substituting Eq. (2) into Eq. (1), we have

$$\begin{aligned}\mathcal{S}_1 &= \{\mathbf{R}(N,\boldsymbol{u}_1)\}\cdot\{\mathbf{R}(N,\boldsymbol{v}_1)\}\cdot\{\mathbf{R}(N,\widehat{\boldsymbol{nc}_1})\}\cdot\{\mathbf{R}(C_1,\boldsymbol{j}_1)\}\\ &\quad\cdot\{\mathbf{R}(C_1,\boldsymbol{k}_1)\}\\ &= \{\mathbf{S}(N)\}\cdot\{\mathbf{S}(C_1)\}\end{aligned} \tag{3}$$

given that $\{\mathbf{R}(N,\widehat{\boldsymbol{nc}_1})\}=\{\mathbf{R}(N,\widehat{\boldsymbol{nc}_1})\}\cdot\{\mathbf{R}(N,\widehat{\boldsymbol{nc}_1})\}=\{\mathbf{R}(N,\widehat{\boldsymbol{nc}_1})\}\cdot\{\mathbf{R}(C_1,\widehat{\boldsymbol{nc}_1})\}$, that is, $\forall x, x\in\{\mathbf{R}(N,\widehat{\boldsymbol{nc}_1})\}\cdot\{\mathbf{R}(N,\widehat{\boldsymbol{nc}_1})\}, x\in\{\mathbf{R}(N,\widehat{\boldsymbol{nc}_1})\}$ and provided that $\boldsymbol{u}_1$, $\boldsymbol{v}_1$, and $\widehat{\boldsymbol{nc}_1}$ are linearly independent vectors, as it is the case in general position. It is important to note here that $\mathcal{S}_1$ contains the subgroup $\{\mathbf{R}(N,\widehat{\boldsymbol{nc}_1})\}$ used in the reduction above.

Applying the same reduction to the nodes 1, 4, 5, and 6, we get

$$\mathcal{S}_2 = \{\mathbf{S}(N)\}\cdot\{\mathbf{S}(C_2)\} \tag{4}$$

For the case of the set of nodes 1, 6, 7, and 8, we have (with $\boldsymbol{u}_3 \parallel \boldsymbol{v}_3 \parallel \boldsymbol{y}$)

$$\begin{aligned}\mathcal{S}_3 &= \{\mathbf{R}(A_3,\boldsymbol{u}_3)\}\cdot\{\mathbf{R}(B_3,\boldsymbol{v}_3)\}\cdot\{\mathbf{S}(C_3)\}\\ &= \{\mathbf{R}(A_3,\boldsymbol{y})\}\cdot\{\mathbf{R}(B_3,\boldsymbol{y})\}\cdot\{\mathbf{S}(C_3)\}\end{aligned} \tag{5}$$

Since the subgroup $\{\mathbf{R}(C_3,\boldsymbol{y})\}$ is a proper subset of the subgroup $\{\mathbf{S}(C_3)\}$, that is, $\{\mathbf{R}(C_3,\boldsymbol{y})\}\subset\{\mathbf{S}(C_3)\}$, then, by the property of closure in groups, we get $\{\mathbf{R}(C_3,\boldsymbol{y})\}\cdot\{\mathbf{S}(C_3)\} = \{\mathbf{S}(C_3)\}(\forall x, x\in\{\mathbf{R}(C_3,\boldsymbol{y})\}\cdot\{\mathbf{S}(C_3)\}, x\in\{\mathbf{S}(C_3)\})$. Hence

$$\begin{aligned}\mathcal{S}_3 &= \{\mathbf{R}(A_3,\boldsymbol{y})\}\cdot\{\mathbf{R}(B_3,\boldsymbol{y})\}\cdot\{\mathbf{R}(C_3,\boldsymbol{y})\}\cdot\{\mathbf{S}(C_3)\}\\ &= \{\mathbf{G}(\boldsymbol{y})\}\cdot\{\mathbf{S}(C_3)\}\end{aligned} \tag{6}$$

where $\{\mathbf{G}(\boldsymbol{u})\} = \{\mathbf{R}(O,\boldsymbol{u})\}\cdot\{\mathbf{R}(P,\boldsymbol{u})\}\cdot\{\mathbf{R}(Q,\boldsymbol{u})\}$, with $O\neq P\neq Q$, corresponds to the subgroup of planar gliding motions determined by the unit normal vector $\boldsymbol{u}$. In this case, $\mathcal{S}_3$ must contain the subgroup $\{\mathbf{R}(C_3,\boldsymbol{y})\}$.

$\mathcal{S}_1$, $\mathcal{S}_2$, and $\mathcal{S}_3$ are kinematic constraints defined as subsets of the group of rigid-body displacements that result from the composition operation of the subgroups involved in their corresponding nodes. After these three serial operations, the original graph of kinematic constraints is reduced to a graph of two nodes with three edges as shown in Fig. 3(*b*).

For simplifying the three kinematic constraints of the current reduced graph to a single couple of edges, we apply parallel reduction—i.e., to compute the intersection of the kinematic constraints associated to two edges—to, for instance, the kinematic constraints $\mathcal{S}_1$ and $\mathcal{S}_2$, and $\mathcal{S}_2$ and $\mathcal{S}_3$. The intersection ($\cap$) of two kinematic constraints is basically the intersection as in set theory, taking into account that the intersection of some subgroups generates a subgroup besides the identity displacement, which is equivalent to the rigid connection between bodies. For instance, the intersection between a spherical rotation $\{\mathbf{S}(N)\}$ and a planar gliding motion $\{\mathbf{G}(\boldsymbol{u})\}$ is $\{\mathbf{R}(N,\boldsymbol{u})\}$. Similarly, $\{\mathbf{S}(O)\}\cap\{\mathbf{S}(P)\} = \{\mathbf{R}(O,\widehat{\boldsymbol{op}})\} = \{\mathbf{R}(P,\widehat{\boldsymbol{op}})\}$ with $\widehat{\boldsymbol{op}} = \mathbf{OP}/\|\mathbf{OP}\|$. It is important to note that introduction of new subgroups during serial reductions (as it was done in the examples above) may limit the set of possible subgroups resulting from intersections.

For the case of the kinematic constraints $\mathcal{S}_1$ and $\mathcal{S}_2$, we have

$$\begin{aligned}\mathcal{P}_1 &= \mathcal{S}_1\cap\mathcal{S}_2\\ &= \{\mathbf{S}(N)\}\cdot\{\mathbf{S}(C_1)\}\ \cap\ \{\mathbf{S}(N)\}\cdot\{\mathbf{S}(C_2)\}\\ &= \{\mathbf{S}(N)\}\cdot(\{\mathbf{S}(C_1)\}\cap\{\mathbf{S}(C_2)\})\\ &= \{\mathbf{S}(N)\}\cdot\{\mathbf{R}(C_1,\widehat{\boldsymbol{c}_1\boldsymbol{c}_2})\}\end{aligned} \tag{7}$$

For $\mathcal{S}_2$ and $\mathcal{S}_3$, we get

$$\begin{aligned}\mathcal{P}_2 &= \mathcal{S}_2\cap\mathcal{S}_3\\ &= \{\mathbf{S}(N)\}\cdot\{\mathbf{S}(C_2)\}\ \cap\ \{\mathbf{G}(\boldsymbol{y})\}\cdot\{\mathbf{S}(C_3)\}\\ &= \{\mathbf{R}(N,\boldsymbol{y})\}\cdot\{\mathbf{R}(N,\widehat{\boldsymbol{nc}_3})\}\cdot\{\mathbf{R}(C_2,\boldsymbol{y})\}\cdot\{\mathbf{R}(C_2,\widehat{\boldsymbol{c}_2\boldsymbol{c}_3})\}\\ &= \{\mathbf{R}(N,\boldsymbol{y})\}\cdot\{\mathbf{R}(N,\widehat{\boldsymbol{nc}_3})\}\cdot\{\mathbf{S}_2(C_2)\}\end{aligned} \tag{8}$$

where $\{\mathbf{S}_2(O)\} = \{\mathbf{R}(O,\boldsymbol{u})\}\cdot\{\mathbf{R}(O,\boldsymbol{v})\}$ is the submanifold included in $\{\mathbf{S}(O)\}$ defined as the composition of two different subgroups of rotations whose axes meet at a single point [17]. Now, let $\widehat{\boldsymbol{nc}_2}$ a unit vector that is parallel to the line defined by points N and C_2, and $\boldsymbol{j}_2$ a unit vector that is linearly independent to it. Then, likewise as in the case of Eq. (2), we have

$$\begin{aligned}\{\mathbf{S}_2(C_2)\} &= \{\mathbf{R}(C_2,\widehat{\boldsymbol{nc}_2})\}\cdot\{\mathbf{R}(C_2,\boldsymbol{j}_2)\}\\ &= \{\mathbf{R}(N,\widehat{\boldsymbol{nc}_2})\}\cdot\{\mathbf{R}(C_2,\boldsymbol{j}_2)\}\end{aligned} \tag{9}$$

Replacing Eq. (11) into Eq. (8), we get

$$\begin{aligned}\mathcal{P}_2 &= \{\mathbf{R}(N,\boldsymbol{y})\}\cdot\{\mathbf{R}(N,\widehat{\boldsymbol{nc}_3})\}\cdot\{\mathbf{R}(N,\widehat{\boldsymbol{nc}_2})\}\cdot\{\mathbf{R}(C_2,\boldsymbol{j}_2)\}\\ &= \{\mathbf{S}(N)\}\cdot\{\mathbf{R}(C_2,\boldsymbol{j}_2)\}\end{aligned} \tag{10}$$

provided that $\boldsymbol{y}$, $\widehat{\boldsymbol{nc}_3}$, and $\widehat{\boldsymbol{nc}_2}$ are linearly independent vectors, as it is the case in general position. Note that Eqs. (7) and (10) correspond to a four-manifold, as it is required by the closed kinematic chain associated to the kinematic constraints $\mathcal{S}_1$ and $\mathcal{S}_2$, and $\mathcal{S}_2$ and $\mathcal{S}_3$, respectively.

After the application of the two presented parallel reductions, a graph of kinematic constraints of two nodes with two edges is obtained. The nodes of such graph are the base of the spherical hand and the grasped object, both connected by the kinematic constraints $\mathcal{P}_1 = \mathcal{S}_1 \cap \mathcal{S}_2$ and $\mathcal{P}_2 = \mathcal{S}_2 \cap \mathcal{S}_3$. To get the final subset of displacements of the grasped object, a last parallel reduction is applied to the constraints $\mathcal{P}_1$ and $\mathcal{P}_2$, as shown in Fig. 3(*c*). Thus, we have

$$\begin{aligned}\mathcal{P}_3 &= \mathcal{P}_1 \cap \mathcal{P}_2 \\ &= \{\mathbf{S}(N)\} \cdot \{\mathbf{R}(C_1, \widehat{\boldsymbol{c}_1\boldsymbol{c}_2})\} \cap \{\mathbf{S}(N)\} \cdot \{\mathbf{R}(C_2, \boldsymbol{j}_2)\} \\ &= \{\mathbf{S}(N)\} \cdot (\{\mathbf{R}(C_1, \widehat{\boldsymbol{c}_1\boldsymbol{c}_2})\} \cap \{\mathbf{R}(C_2, \boldsymbol{j}_2)\}) \\ &= \{\mathbf{S}(N)\}\end{aligned} \tag{11}$$

since $\{\mathbf{R}(C_1, \widehat{\boldsymbol{c}_1\boldsymbol{c}_2})\} \cap \{\mathbf{R}(C_2, \boldsymbol{j}_2)\} = \{\mathbf{I}\}$, the identity displacement.

Equation (11) implies that the feasible movements of a grasped object by the spherical hand with two-link thumb of static base correspond in general to a spherical rotation about N, the intersection point of the revolute axes of the curved fingers. This finite spherical motion is a three-manifold, as it is required by the mobility of the associated kinematic chain of the hand-object system. By repeating the above analysis, locking the action of the proximal joints, it can be verified that the spherical motion can be fully controlled by the hand actuators since the resulting displacement is the identity.

2.2 Alternative Thumbs. Section 2.1, detailed the kinematic reduction for the spherical hand with the *two-link, no-pivot* (NP) thumb, the conventional design where the proximal joint at the base has a single degree of freedom. Figure 4 shows the kinematic models for other thumb variations herein proposed to improve upon the functionality achieved in the authors' initial study [18]. The primary difference is the addition of a *pivot* (P), orthogonal to the flexion rotation axes, at the thumb base allowing the finger to swing side to side. Thus, the spherical hand morphologies include the curved fingers with a conventional two-link thumb of static base as well as the curved fingers with both a *two-link, pivot* (2P) thumb and a *one-link, pivot* (1P) thumb. Mechanical design details for the modified base are provided in Sec. 3.3.

It can be shown that the serial reduction for the two-link pivot thumb (Fig. 4(*b*)) is $\mathcal{S}_3 = \{\mathbf{D}\}$, the continuous group of displacements corresponding to a six-manifold. Then, the resulting displacement of a grasped object by the spherical hand with two-link pivot thumb (2P) is the intersection of the curved finger kinematic constraints, $\mathcal{P}_1 = \mathcal{S}_1 \cap \mathcal{S}_2 = \{\mathbf{S}(N)\} \cdot \{\mathbf{R}(C_1, \widehat{\boldsymbol{c}_1\boldsymbol{c}_2})\}$, which is the composition of a spherical motion about the common center N and a rotation about the axis defined by the fingertips of the curved fingers. However, in this case, the rotation about the fingertips is controllable and there always exists a line on such an object with motion constrained on a sphere centered on N despite the additional degree of freedom.

Likewise, the motion for the *one-link, pivot* (1P) thumb (Fig. 4(*c*)) is described by $\mathcal{S}_3 = \{\mathbf{R}(A_3, \boldsymbol{u}_3)\} \cdot \{\mathbf{R}(P_3, \boldsymbol{w}_3)\} \cdot \{\mathbf{S}(C_3)\}$, which can be reduced to

$$\mathcal{S}_3 = \{\mathbf{R}(A_3, \boldsymbol{u}_3)\} \cdot \{\mathbf{R}(P_3, \boldsymbol{w}_3)\} \cdot \{\mathbf{R}(C_3, \boldsymbol{w}_3)\} \cdot \{\mathbf{S}(C_3)\} = \{\mathbf{D}\} \tag{12}$$

where $\{\mathbf{D}\}$ must contain the subgroup $\{\mathbf{R}(C_3, \boldsymbol{w}_3)\}$ and $\boldsymbol{w}_3$ is the same rotation axis as that for the thumb base pivot. $\mathcal{P}_2$ then resolves to $\{\mathbf{S}(N)\} \cdot \{\mathbf{R}(C_2, \boldsymbol{j}_3)\}$ where $\boldsymbol{j}_3$ is some vector linear independent to $\boldsymbol{w}_3$, and consequently, the final reduction for $\mathcal{P}_3$ is the same as that for the standard two-link, no-pivot (NP) thumb design, that is, the feasible movements of a grasped object by the spherical hand with one-link, pivot (1P) thumb correspond in general to a spherical rotation about N.

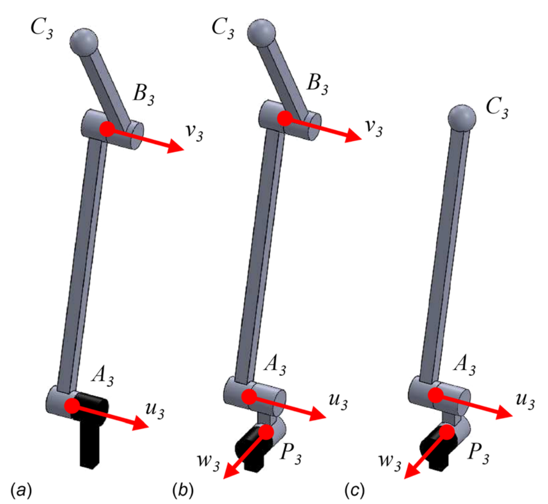

Fig. 4 Structure of thumb designs of the spherical hands: (*a*) two-link thumb with static base, (*b*) two-link thumb with pivot base, (*c*) one-link thumb with pivot base

3 Mechanical Implementation

An initial evaluation of in-hand workspace in underactuated hands used two-link, linear, underactuated fingers with a revolute, proximal joint and a flexure-based distal joint [19]. An open-source, three-finger hand design [20] based on that work serves as the experimental hardware platform to evaluate the effects of mechanical design modifications on manipulation capabilities. All fingers are modular, each is driven by a single agonist tendon, and the distal flexure joints were replaced by revolute joints to match the model presented in Sec. 2.

3.1 Curved Fingers. To satisfy the design constraints of the spherical hand morphologies, an out-of-plane angular offset of $\pi/4$ rad was applied to the middle of the link in the prototype implementation, as shown in Fig. 5(*a*). This angle can be modified to adjust the offset of the joint axes' intersection relative to the finger base. To ensure that joint axes intersection for one curved

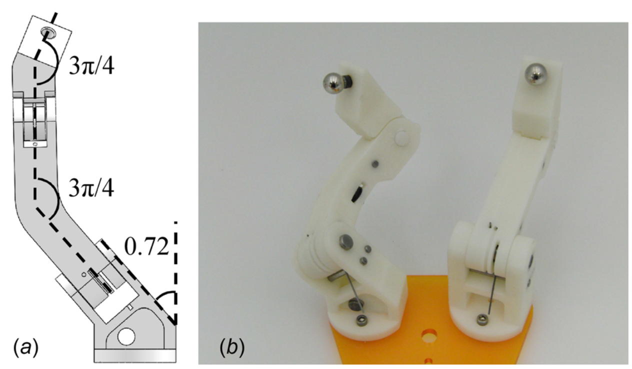

Fig. 5 (*a*) Proposed design of the prototype curved fingers, and (*b*) physical comparison of the curved fingers from the spherical hand designs with the standard, planar fingers used in traditional hand designs. Other finger link geometries are possible as long as the joint axes' intersection is maintained.

finger can be coincident with that of the other corresponding finger in the pair, the intersection offset projected onto the palmar surface needs to be at least 1/2 the distance between the finger bases. For consistency, the distal phalanx also uses the same angular offset, though the designer is free to implement any arbitrary offset from the distal joint to the fingertip without affecting the joint axes intersection. The curved finger bases were tilted by 0.72 rad to accommodate power grasping, as suggested by past work [18]. Note that the out-of-plane angular offset does not need to be implemented as a continuous curve between the joints. In fact, an alternative finger link geometry may be more optimal for other grasping scenarios.

Figure 5(*b*) shows a side-by-side comparison of the curved finger design for the spherical hands with the traditional linear design used in the authors' previous works. For both, the effective lengths for the overall finger, proximal link, and distal link were 100 mm, 62.5 mm, and 37.5 mm, respectively, consistent with the optimal parameters chosen in prior underactuated hand designs [18].

3.2 Hand Layout. The proposed finger designs can be arranged such that the common center N is situated either within the hand workspace or outside. While the former can be preferable to the latter, a closing force on the object is only possible for the latter due to the free-swing trajectories of the tendon-actuated finger, as shown in Fig. 1. In this study, the in-hand manipulation capabilities were only evaluated for discrete, static base configurations, such that the effective common center N was invariant. Grasp stability requirements may necessitate coupled motions between the base and individual fingers for desired task primitives, although that would then affect the location of the common center N.

3.3 Thumb Base Design. The authors' prior work on spherical hand designs [18] and results from related human studies [21] suggest that thumb mobility greatly impacts the achievable in-hand workspace. Considerable research efforts have been applied to opposable thumb design in anthropomorphic hands [13,14]. Qualitatively, past work in underactuated hands with flexural joints [19] suggested having an additional passive axis of rotation orthogonal to the standard design's joint axes, which are traditionally parallel with one another, could aid in pinch grasp adaptability and stability. Figure 6 illustrates the design changes made to the thumb base, providing a passive axis of rotation and allowing the thumb to swing side-to-side. This pivot is anchored to the base with a pair of extension springs, and its behavior is independent of the thumb actuation, since the actuating tendon runs through the axis center. When not in contact with an object or an opposing finger, this joint axis would be inactive, and the thumb would have the same free-swing behavior as the standard thumb design without the additional joint axis in its base. An articulated thumb base is generally reserved for high-complexity and fully actuated hands with actuators situated outside of the main hand structure [14]. The passive pivot introduced in this study may provide a useful alternative for low and medium-complexity hands without compromising performance or packaging. This modification is implemented in both the spherical hand with two-link, pivot thumb (2P) and the spherical hand with one-link, pivot thumb (1P), as detailed in Sec. 2.2.

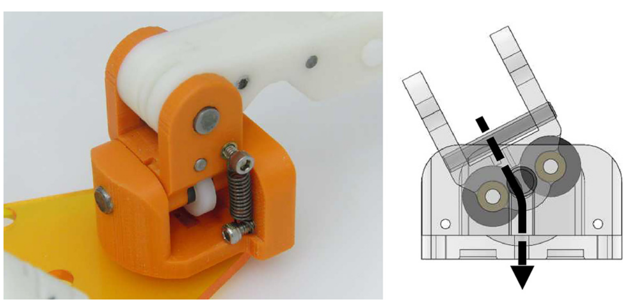

Fig. 6 The passive, pivoting degree of freedom is implemented such that it is not actuated by the main drive tendon. The drive tendon passes through the rotational axis of the pivot. Extension springs on both sides of the finger base set the initial configuration at center.

4 Ideal Kinematic Workspace

In this section, we seek to experimentally examine the "ideal" kinematic workspace of the robot hands, that is, the range of object positions/orientations that can be achieved outside of the constraints of needing force closure on the grasped body. Instead of relying on simulation, this is achieved by using an object with magnetic contacts that accommodate steel spheres at the hand's fingertips.

4.1 Experimental Setup. Manipulation models, including the one described in Sec. 2, often assume simplified contact models that can be difficult to replicate in a physical real-world system. To validate the common center predicted by the spherical hand morphologies, we first introduce an experimental setup that maintains ideal point contact constraints through the use of magnetic spherical joints, as described in Figs. 7(*b*) and 7(*c*). A cylindrical magnet and a countersunk nylon washer are embedded at each contact location in a test object, and a steel sphere is affixed to the distal end of each finger. This creates a consistent spherical joint, the kinematic equivalent of point contact with friction, at the

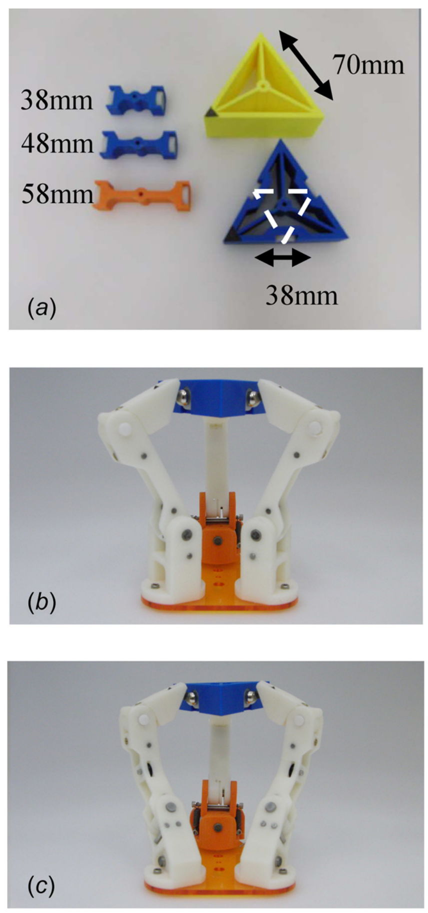

Fig. 7 Manual, unactuated exploration of the reachable kinematic spaces for the standard (*b*) and (*c*) spherical hand designs was explored for both two-finger and three-finger contact conditions and a variety of object sizes (*a*)

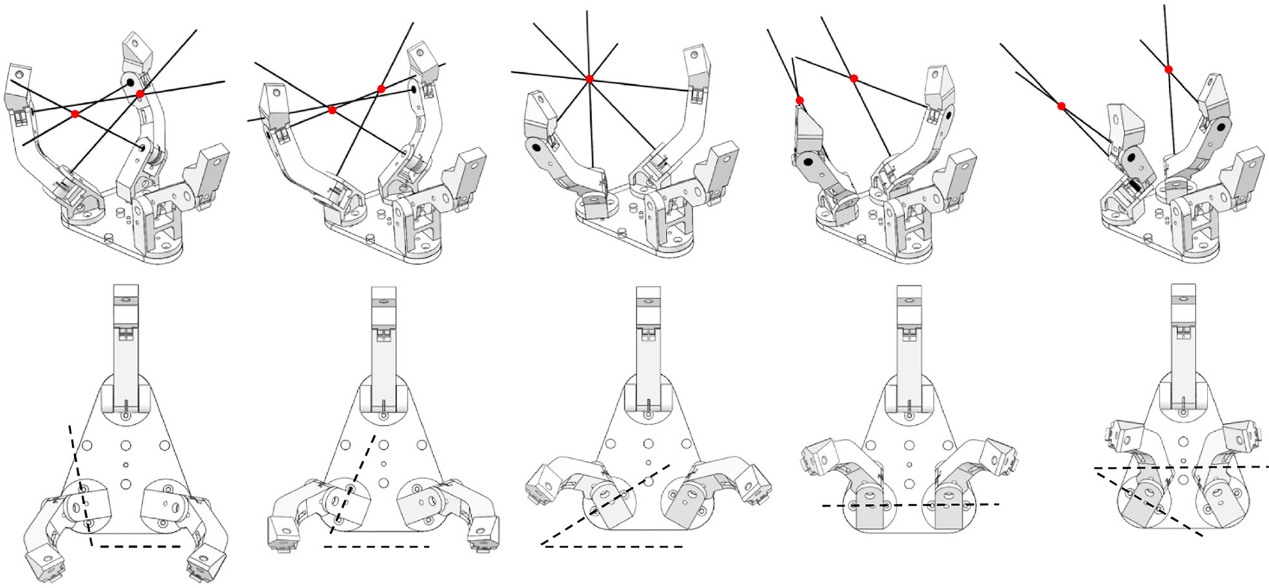

Fig. 8 Set of discrete base configurations that were tested for both the standard and spherical hand fingers. Configuration C is considered to be the ideal spherical hand case, where the joint axes all intersect at a common point.

finger-object interface. A trakSTAR [22] position sensor was affixed to the center of the test object to track its Cartesian position and orientation. The sensor has spatial resolution of 0.5 mm and orientation resolution of 0.002 rad.

This experimental setup was unactuated but used the same physical finger links and base spacing as the final spherical hand prototypes. The spherical magnet at each fingertip engaged directly with the object. The base orientation for the curved fingers could be set to five different discrete configurations, as shown in Fig. 8. These configurations account for the full range of finger base rotation possible in the robotic prototype to be described in Sec. 5. According to the computer aided design model, configuration C, with the base offset 0.514 rad (29.5 deg) from horizontal, generates the ideal scenario, with the joint axes intersecting at the desired common center N. To evaluate the achievable workspace, the object-hand test setup was manually reconfigured by the authors. For each finger type, base configuration, and test object, three trials were performed, and in each trial, 2000 pose measurements were recorded at the trakSTAR system's default measurement rate, approximately 30 Hz.

Figure 7(*a*) shows the range of objects used in this evaluation. Two-contact bar objects of lengths 38 mm, 48 mm, and 58 mm, and a three-contact triangular object with side-length 70 mm, contact-spacing length 38 mm was used to measure the achievable workspace. The two-contact bar objects were used to measure the manipulation behavior of the curved fingers. In the case of the spherical hand designs, these two fingers primarily dictate the final shape of the object workspace. Although just a single pair of fingers may be insufficient for a stable precision grasp, the kinematic workspace for the linkage chain corresponding to the two-finger case encompasses that of the three-finger case and provides a larger workspace from which to extract insight.

Note that there is an unconstrained axis of rotation for the two-contact bar objects—corresponding to the rotation about the axis defined by the contact points, so only the Cartesian position data were considered in those tests, and the sensor was affixed such that the free rotation did not generate Cartesian errors.

4.2 Workspace Evaluation. A hybrid statistical, k-nearest-neighbors (KNN) approach similar to the statistical outlier filter implemented in the point cloud library (PCL) [23] was used to remove outliers from the measured dataset. For each point p_i in set P, the algorithm calculates the distances to the k nearest neighbors, D_i,where $k = \sqrt{n}$, and n is the size of the dataset. The maximum such distance for each point, $\max(D_i)$, was recorded in set $D_{\max}$, and points p_i with $\max(D_i)$ outside the range $\mathrm{mean}(D_{\max}) \pm 1.96\ \mathrm{std}(D_{\max})$ were removed. This algorithm is independent of coordinate-frame selection, does not bias the resulting workspace toward any shape or convexity, and still performs well for sparse datasets.

To calculate the workspace volume and shape from the manual trials, the authors used alpha shapes [24] to account for concave workspace volumes. The principal axes were also found to provide useful comparisons to past human manipulation studies [21]. The alpha shape volume was determined with an alpha radius equivalent to the standard deviation of points along the minimal principal axis. Angular workspace is presented in terms of Cayley–Rodriguez coordinates, components of the vector u satisfying $R = \exp(\widehat{u}) = I + (\widehat{u}/|u|)\sin|u| + (\widehat{u}^2/|u|^2)(1 - \cos|u|)$, where R is the rotation matrix.

To approximate the common workspace center, if it exists, a voxel binning filter as described in Ref. [21] with 2 mm grid spacing was first used to remove any bias from nonuniform workspace sampling. The common center for each dataset P was then determined by finding the point p_c in discretized task space satisfying $\mathrm{argmin}_{p_c}(\mathrm{std}(\mathrm{Dist}(P, p_c)))$, that is, the point for which the standard deviation of the distances between that point and all points in the dataset is minimal. Least-squares solutions for approximating the workspace center [25] were insufficient, due to the limited range of motion for the tracked object. The calculated center was not recorded if the radius was found to be greater than 500 mm. The Cartesian errors (mm) to the workspace center predicted by the computer aided design model for the ideal spherical configuration (C) were also calculated.

4.3 Experimental Results. An example comparison of the workspaces for the spherical and standard hand designs' two opposition fingers is presented in Figs. 9 and 10. Each set of plots show the raw trakSTAR position data for the instrumented object, collected during manual exploration. The shell-like form of the

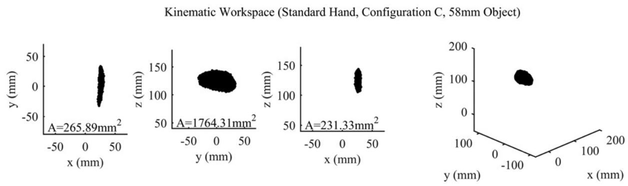

Fig. 9 Experimentally sampled workspace projections for the standard hand, for base configuration C and test object size 58 mm, utilizing an ideal kinematic setup with magnetic spherical joints

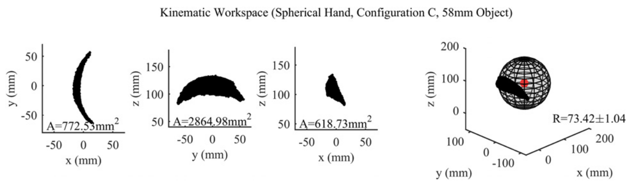

Fig. 10 Experimentally sampled workspace projections for the spherical hand, for base configuration C and test object size 58 mm. The spherical surface fitting is more consistent for the spherical hand configuration than traditional hand designs.

object workspace in the spherical hand case—utilizing the two curved fingers—is readily evident from the 2D projections of the point cloud from these experimental trials using the magnetic kinematic setup, and the workspace fitted to a spherical surface is shown in Fig. 10.

Note that by using magnetic contacts to represent idealized point contacts, this study on kinematic reachability does not consider the hand's ability to produce a stable grasp in each reachable pose. The magnetic contacts also generate a higher effective friction cone than what would be possible with a physical hand. However, the combined workspace can be used to validate the common center proposed by the spherical hand concept.

The workspace from a two-finger standard hand design should result in a common center at infinity in an ideal system, since the joint axes for each finger are parallel, and as Table 1 shows, the majority of the standard hand configurations could not produce a common center within 500 mm of the workspace dataset. In contrast, kinematic workspaces from spherical hand configurations could all be fitted to spherical surfaces with radii in the range [40,90] mm.

Across the three evaluated object sizes, the workspace center was most consistent for spherical fingers in the C and D base configurations, according to the variance of the measured Cartesian errors. Unexpectedly, configuration D produced more consistent workspace centers, contrary to the model's expectations. This may be due to a special condition in configuration D, where the corresponding distal and proximal joint axes between fingers are parallel. For both configurations, the workspace center varied by less than 5 mm across all test cases.

Table 2 summarizes the ideal workspace results for the three-finger contact condition, using configuration C and the proposed thumb design options, for both the standard and spherical cases. The measured workspaces should be a subset of those recorded from the two-finger contact condition. In the cases with the two-link thumb with static base (NP), it was not possible to extract the expected common center from limited workspace point cloud, from either hand design. The static base limits the achievable workspace, and calculating the center for smaller experimental workspaces is more sensitive to measurement noise and remaining outliers.

Values calculated for the human manipulation workspace as measured by Bullock et al. [21] are included for comparison in both Tables 1 and 2. Their study utilized circular test objects with diameter between 33 and 40 mm and full mobility of the human hand. Cells are highlighted for cases where the experimental values in our test setup exceeded the human manipulation performance. With static finger bases and fewer joints, the curved fingers in the manual setup could reach a larger workspace, while the standard planar fingers could not. This may suggest that nonparallel joint axes could be beneficial in increasing workspace size, in addition to generating unique characteristics to the overall topology.

In terms of Cartesian workspace size, the spherical hand outperforms the standard hand for nearly all configurations and object sizes in the two-finger contact condition. For example, in configuration C, the base configuration satisfying the desired spherical hand constraints, the standard hand design could only achieve

Table 1 Two-finger ideal kinematic workspaces

Type	Config.	Obj. size (mm)	Radius (mm)	Cart. err. (mm)	Alpha vol (cm^3)	PCA 1 (cm)	PCA 2 (cm)	PCA 3 (cm)
Human		33–40	—	—	5.7	4.06	2.23	1.01
Standard	C	58	231.84 ± 1.17	279.76	4.71	5.81	3.70	0.50
		48	193.71 ± 1.13	243.76	2.00	4.38	3.90	0.46
		38	26.30 ± 2.38	79.91	5.35	4.03	3.38	0.59
	D	58	—	—	0.622	20.89	**10.02**	0.34
		48	—	—	1.95	17.30	7.40	0.40
		38	—	—	5.86	18.08	8.34	0.64
	E	58	—	—	5.70	7.95	4.32	0.64
		48	—	—	4.04	6.54	3.98	0.61
		38	—	—	7.30	4.82	3.71	0.76
Spherical	A	58	76.56 ± 1.13	47.76	1.89	3.21	2.11	0.47
		48	42.75 ± 0.97	83.72	0.77	2.57	1.69	0.43
	B	58	71.99 ± 1.24	30.15	4.02	4.21	3.65	0.64
		48	75.70 ± 1.20	29.78	4.22	4.51	4.05	0.58
		38	68.53 ± 1.06	45.75	3.73	4.47	4.31	0.63
	C	58	73.42 ± 1.04	16.90	8.50	10.10	4.29	2.06
		48	78.29 ± 0.92	14.31	8.88	11.80	5.36	2.06
		38	73.65 ± 1.46	18.72	**14.94**	11.87	5.43	2.00
	D	58	87.48 ± 0.64	9.55	6.10	12.04	4.87	2.18
		48	86.19 ± 0.72	11.04	8.08	11.88	4.53	2.01
		38	80.90 ± 1.09	11.18	13.91	**12.60**	4.65	**2.10**
	E	58	77.57 ± 0.76	15.86	4.70	9.41	5.00	1.31
		48	74.06 ± 0.92	17.93	5.48	7.71	4.65	1.09
		38	62.54 ± 1.28	27.52	6.31	6.02	4.51	0.84

Values greater than the corresponding human value are highlighted, and the maximum value for each workspace metric is bolded.

Table 2 Three-finger ideal kinematic workspaces (configuration C)

Type	Thumb	Radius (mm)	Cart. err (mm)	Alpha vol (cm^3)	PCA 1 (cm)	PCA 2 (cm)	PCA 3 (cm)
Human		—	—	4.8	3.62	2.01	0.96
Standard	No-pivot (NP)	—	—	0.64	3.15	0.68	0.40
	P, one-link 70 mm	189.68 ± 1.54	244.99	2.44	3.56	1.38	0.62
	P, two-link 85 mm	—	—	4.39	4.27	2.06	0.65
	P, two-link 100 mm	—	—	4.62	4.40	3.00	0.59
Spherical	NP	33.94 ± 1.22	69.93	1.04	3.19	0.89	0.51
	P, one-link 70 mm	65.30 ± 0.92	45.67	2.30	6.92	1.43	0.97
	P, two-link 85 mm	93.85 ± 1.23	9.48	7.42	**10.11**	**2.98**	**1.10**
	P, two-link 100 mm	95.47 ± 1.38	6.59	**7.76**	9.67	2.86	1.09

Values greater than the corresponding human value are highlighted, and the maximum value for each workspace metric is bolded.

37%, 42%, and 72% of the spherical hand's alpha volume, primary principal axis, and secondary axis, respectively. For the spherical hands, using configuration C also resulted in the largest overall workspaces, averaged across all the test objects. Configuration D, where the fingers are in direct opposition, presented a special case where the standard hand workspace was predominantly planar, resulting in large primary and secondary principal axes, but a low overall workspace volume. In contrast, it should be noted that the two-finger spherical hand cannot achieve a purely planar workspace without coordinated base motion.

For the spherical hands, the design incorporating the additional thumb base pivot and a 2DOF thumb (100 mm) resulted in the largest Cartesian and angular workspaces, as shown in Table 2, as well as a spherical surface fit with the calculated center closest to the theoretical common center found via the CAD model (<10 mm). However, the standard hand design was able to reach larger overall Cartesian and angular workspaces with the same thumb design (two-link, pivot thumb), exceeding both conservative measures of the human manipulation workspace from Ref. [21] for three-finger grasps.

5 Experimental Manipulation Workspaces

Although the unactuated kinematic test setup in Sec. 5 corroborated the spherical workspace center and the kinematic performance of the fingers designed for the spherical hands, it did not assess the effect of the new finger design and layout on grasp capability when compared to past work on underactuated precision manipulation [19]. The point contact assumption is difficult to reproduce in physical, in-hand manipulation trials, which generally require rolling [26] or soft contacts [27]. In this section, we present a simplified model for precision-grasp stability in underactuated hands, with the assumption that reconfiguring, underactuated fingers behave like elastic springs. We also detail the implementation of passive, rotary fingertips, designed such that under no-slip conditions, the object-finger interface will not exhibit rolling, allowing the hand to leverage the advantages of soft contacts without needing to account for its behavior in control.

5.1 Underactuated Grasp Stability. Due to passive reconfiguration, underactuated hands typically cannot satisfy the conditions for full force closure. Instead, relevant work [28] focuses on the hand's ability to produce equilibrium grasps, where

$$\dot{\xi}_{\text{object}} = J\dot{q} \tag{13}$$

$$-J^T w = \tau \tag{14}$$

For object twist $\dot{\xi}_{\text{object}}$, system Jacobian J can be calculated for the hand-object system described in Sec. 2.1 [29], finger joint configurations $\boldsymbol{q}$, finger joint torques τ, and an external wrench w, which should include at least the effects of gravity on the object mass. A potential function $V(\boldsymbol{q})$ exists for a grasped object at equilibrium such that $\Delta V(\boldsymbol{q}) > 0$ for nonzero joint configuration displacements $\Delta \boldsymbol{q}$ [30].

In practice, the authors have achieved stable precision grasps with underactuated hands through position-control of the actuation tendon lengths for each finger without tactile or visual feedback [19,31]. The generated grasp force is a result of the fingers' reconfiguration from their free-swing trajectory due to the object contact constraints, as shown in Fig. 11. The free-swing configuration ${}^f\boldsymbol{q_i}$ for the ith finger and some actuation tendon length a_i is determined by

$$\text{argmin}_{q_i}\left({}^fE_i\right) = \text{argmin}_{q_i}\left(\frac{1}{2}\sum_{j=1}^{n_f} k_{ij}(q_{ij} - q_{ij0})\right) \tag{15}$$

$$J_A \Delta q_i = \Delta a_i \tag{16}$$

where E_i is the energy of the ith finger due to the passive joint stiffnesses, ${}^fE_i$ is the free-swing energy of the ith finger in the absence of contact, n_f is the number of joints, k_{ij} is the joint stiffness of the jth joint, and q_{ij0} is the rest configuration of the jth joint. J_A is the actuation Jacobian describing the relationship between the tendon length displacement and the related joint configurations [32]. The allowable kinematic reconfiguration for the tendon-driven fingers used in this study is set by the effective pulley radii r_{ij} at each joint [28].

In underactuated two-link fingers, the fingertip point C_i can move along some curve determined by the system's mechanical

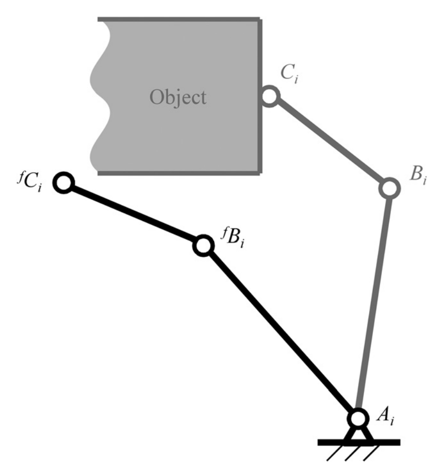

Fig. 11 For a constant tendon actuation length, the passive reconfiguration of the underactuated finger from its free swing trajectory (fCi) to its contact location on the object (Ci) determines the passive set of forces exerted onto the object

design parameters. For contact forces of the relatively small magnitudes found in precision grasps of small objects, it can be assumed that the actuators can hold the commanded tendon positions, especially if they are nonbackdriveable or have high gear ratios. In these cases, each underactuated finger can be simplified as some passive spring with force output:

$$F_i = -\nabla(E_i - {}^f E_i) \tag{17}$$

Consequently, each stable precision grasp configuration can be described as a passive closure constraint as introduced by Yoshikawa [33], where the joint actuation force of the constraining mechanism does not need to be actively controlled. The performance of a similar hand mechanism is described by Hanafusa and Asada [34]. Similarly, Maeda et al. [35] have proposed a hand composed of rigid and soft components where the user only needed to formulate a caging configuration with the former while grasp stability is passively determined by the latter. The achievable object workspace of the underactuated hands presented in this study is determined by the set of actuation tendon lengths that can produce stable precision grasps.

5.2 Rotary Fingertip Design. The hand-object model detailed in Sec. 2 assumes point contact with friction, whose kinematic equivalent is a spherical joint, at the hand-object interfaces. In practice, an idealized point contact with friction is difficult to maintain in physical systems. To help enforce this stable contact assumption and mechanically minimize undesirable rolling and slip, we introduce a passive, rotary fingertip design. A physical point contact simplifies the model by disregarding the effects of local surface curvatures during manipulation. This approach proposes that maintaining the no-slip contact condition is a more robust manipulation strategy than modeling the deformation and rolling behavior of some fingertip with respect to particular object surfaces.

Figure 12 shows the basic components of the rotary fingertip: a cast, soft, urethane shell, a cylindrical magnet press-fit inside the shell, a countersunk nylon washer serving as the low-friction sliding surface of the joint, and a magnetic sphere. The urethane shells were cast in 3D-printed molds using Vytaflex 40 [36], a two-part urethane rubber with shore hardness 40. The magnetic sphere is affixed to an M3 bolt with epoxy and sandwiches the nylon washer against the embedded cylindrical magnet. Using two magnets to sandwich the nylon washer ensures that the fingertip resets to a consistent configuration when not in contact with an object.

Various fingertip geometries, shown in Fig. 13, were evaluated. The *icosahedron* (I) was proposed in the authors' initial work on the spherical hands to maximize the points of contact between the fingertip and object for unknown, local object geometries. The rotary *disk* (D) geometry was introduced to maximize contact with known, flat surfaces and minimize surface rolling. Both rotary (R) and static *round* (SR) geometries were also implemented to provide a control reference.

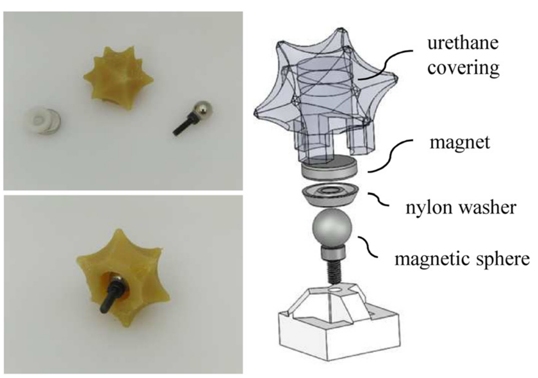

Fig. 12 The rotary fingertips were constructed of a monolithic, cast urethane shell, a neodymium sphere bonded to an M3 bolt, a nylon countersunk washer, and a neodymium disk embedded in the fingertip

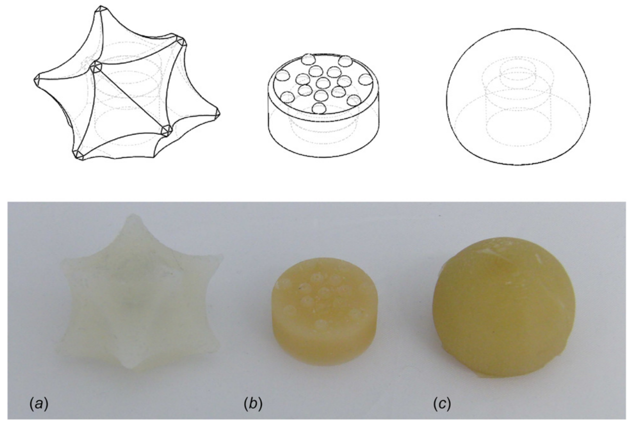

Fig. 13 Multiple fingertip designs were evaluated: (*a*) rotary icosahedron (I), (*b*) rotary disk (D), (*c*) rotary round (R), and static round (SR)

5.3 Experimental Setup. Figure 14 summarizes the test setup used to evaluate the achievable physical workspace of the actuated hands. The triangular test object is the same size as the one used in the unactuated, kinematic experiments, albeit without embedded magnets at the points of contact. The hand is positioned with the palm facing downward so that only precision prehensile grasps are allowed; the object should never be simply resting on the fingertips in a nonprehensile manner. A single trakSTAR sensor was affixed to the center of the object with adhesive.

Figure 15 shows the modifications made to the Model O, an open-source, 3D-printed hand design based on the iHY. The actuated hand used for the experiments incorporates 4 Dynamixel MX-28 servos, 3 of which each drive an underactuated finger via a single tendon. The 4th actuator controls the abduction/adduction between the two nonthumb fingers via a geared transmission and

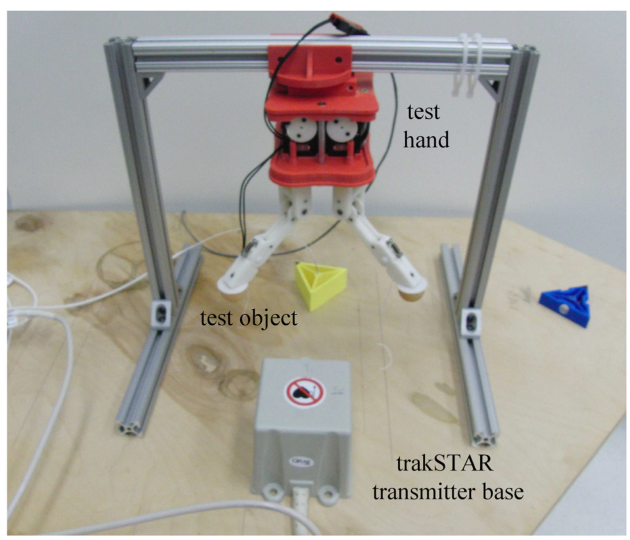

Fig. 14 Test setup for experimental workspace evaluation. The hand is held upside down in a fixture for test grasps and manipulation motions.

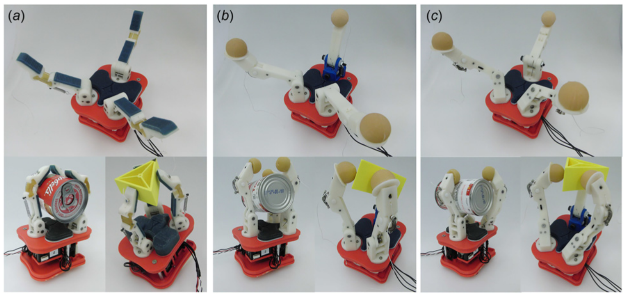

Fig. 15 The design progression from the (*a*) OpenHand Model O, to the (*b*) standard fingers with specialized fingertips, to the (*c*) spherical hand layout, in this case with a two-link thumb of static base

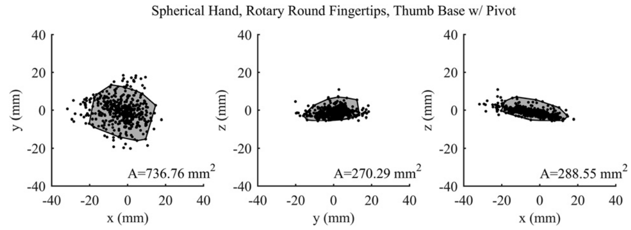

Fig. 16 Experimental manipulation workspace for the spherical hand utilizing rotary round fingertips and a thumb base with pivot providing the additional passive degree of freedom. The light gray overlay shows the calculated alpha shape for the respective projection.

is traditionally used to transition the hand between configurations for power grasping and precision pinch grasping.

The workspace was assessed by discretely exploring the actuation space and recording the motion of the object. The actuation tendon for each finger was adjusted by 1.5 mm increments, and the abduction/adduction base rotation was held static in configuration C to satisfy the spherical hand constraint, shown in Fig. 8. For each target actuation state, the object was first manually placed in the same stable precision grasp in order to keep the manipulation results independent of the grasp acquisition repeatability. The hand was then commanded to each target actuation state and then back to the initial precision grasp. The object pose was recorded if the object did not drop out of a stable grasp configuration, and the Cartesian displacement from the initial and final grasps did not exceed 25 mm.

The object workspace could not be evaluated continuously because grasp stability and contact invariance could not be guaranteed between commanded motions. Past work [18] showed that contact conditions were difficult to maintain, leading to prevalent slip and rolling at the fingertip during motion trials, which is expected for an underactuated hand-object system. However, slip and rolling can be adequately repeatable, resulting in motion primitives that are still useful. The acquired experimental results represent the upper bounds of the achievable mechanical capability of the hand.

Three trials were run for each fingertip design and both pivoting and nonpivoting thumb bases. For the standard hand design, all three fingers were the same size, with overall length 100 mm, proximal link length 62.5 mm, and distal link length 37.5 mm. The spherical hand morphologies use a shorter, 85 mm long thumb, for increased grasp stability, based on qualitative results from the author's initial study on spherical hands [18].

5.4 Experimental Results. Compared to the continuous workspace data from the unactuated, manual test setup, the relatively limited experimental workspace data from the actuated hands is sparser and consequently more susceptible to outliers, even after running the outlier removal algorithm detailed in Sec. 4.2. Projected views for an example workspace dataset are shown in Fig. 16. Workspace volume is reported as both alpha volume and the principle component analysis (PCA) volume, equal to the volume of the ellipsoid formed by the principal axes of the dataset. Alpha volume is particularly sensitive to point cloud outliers, while the PCA ellipsoid assumes a convex workspace and typically only provides an upper bound. The relevant work in human manipulation [21] used voxel binning, which is dependent on the selection of voxel size and also performs best with dense point clouds. Despite these challenges, the experimental results provide a reasonable relative benchmark for evaluating the utility of the finger designs, incorporation of the thumb base pivot, and the different rotary fingertips.

The model predicts that all instantaneous motions are about the predicted common center, and a change in contact conditions merely shifts the object trajectory radially from this center. However, without being able to track the amount of slip or rolling at each contact, the measured workspaces alone were not sufficient to confirm the common center in the spherical hand design. The main goal of this experimental setup with the actuated hand was to determine whether changes to finger curvature and fingertip design would compromise or enhance the achievable in-hand manipulation workspace.

The principal axes and PCA volume for the Cartesian workspaces shown in Table 3 suggest that there is an overall decrease in performance for the spherical hand when compared to the standard hand design. This is consistent for all fingertip and thumb base combinations. This may be largely due to the actuated free-swing trajectory of the curved fingers. For the base configuration used in these tests and with a single actuation tendon per finger, the force output of traditional fingers is always directed toward the center of the hand, but that is not the case for the curved finger design. Despite the simplicity of the hand, the achievable principal components of the measured workspace are not substantially less than those found in human workspaces.

The alpha volume metric suggests the opposite conclusion for certain design parameters. A higher alpha volume, especially for sparse datasets, suggests a greater number of outliers. These outliers are most likely due to slip or rolling conditions. Qualitatively, it was noted that the icosahedron fingertip in particular tended to reconfigure in larger, discrete motions instead of in a continuous manner, due to its geometry. The inclusion of these outliers in the dataset indicates that they are repeatable and minimize the accumulated Cartesian error when returning to the initial pinch pose, but they are still undesirable due to their dependence on the object's material and geometry properties.

The use of standard fingers produced larger principal axes with the pivoting thumb base but had a greater alpha volume with a static thumb base. If the larger alpha volume is indeed due to effects from slip and rolling, then this may suggest that introducing compliant, passive degrees-of-freedom in the finger structure can help compensate for undesirable contact conditions through system reconfiguration. This has been previously proposed in a theoretical framework on dexterous manipulation with underactuated hands [8] and validated in prior experimental evaluations of planar manipulation systems [31].

Of the fingertips designs, all improved upon the baseline Model O design (shown in Fig. 15(*a*)) with fingertips originally designed for power grasping. The rotary disk fingertips augmented the existing design the least. Even with the spherical joint, the disk geometry often did not maintain contact with the object on its singular face. The rotary round fingertip performed well in maximizing the angular workspace (Table 3), particularly in improving the operation of configurations with a static thumb base. Notably, the static round fingertip was not a significant downgrade from the rotary alternatives, especially for the designs using the additional pivot in the thumb base, again indicating that to optimize for robust contact conditions during manipulation, designing for

Table 3 Experimental object workspaces

Thumb	Type	Tip	Alpha vol. (cm^3)	PCA 1 (cm)	PCA 2 (cm)	PCA 3 (cm)	PCA 1 (rad)	PCA 2 (rad)	PCA 3 (rad)
Human (three-finger)			4.8	3.62	2.01	0.96	—	—	—
Model O (unmodified)			0.22	1.09	0.73	0.46	0.24	0.18	0.10
No-pivot	Standard	SR	0.52	1.83	1.24	0.60	0.72	0.43	0.22
		R	0.70	3.03	1.90	0.77	**0.93**	0.36	0.24
		I	0.25	2.60	1.90	0.63	0.56	0.35	0.26
		D	0.30	2.52	1.37	0.81	0.48	0.30	0.22
	Spherical	SR	0.21	1.31	0.85	0.56	0.63	0.36	0.12
		R	0.27	1.56	1.34	0.60	0.74	0.27	0.12
		I	1.20	2.29	1.78	0.74	0.59	0.22	0.18
		D	0.14	1.53	1.33	0.43	0.40	0.24	0.12
Pivot	Standard	SR	0.19	3.76	1.50	0.89	0.68	0.52	0.33
		R	0.10	**4.60**	2.14	0.99	0.65	0.51	0.32
		I	0.16	4.04	2.20	**1.15**	0.72	0.48	**0.35**
		D	0.20	2.81	2.16	0.81	0.45	0.29	0.20
	Spherical	SR	1.36	3.41	**2.92**	0.57	0.82	**0.66**	0.25
		R	0.87	2.97	2.12	0.61	0.64	0.51	**0.35**
		I	1.71	3.14	2.08	0.58	0.77	0.48	0.19
		D	0.26	1.29	1.19	0.43	0.33	0.22	0.12

Values greater than the corresponding human value are highlighted, and the maximum value for each workspace metric is bolded.

reconfiguration through underactuation in the fingers may be a viable alternative to modifying the fingertip complexity.

6 Conclusion

This paper proposed and evaluated underactuated spherical hand morphologies inspired by work in parallel mechanisms to reduce the complexity of planning and executing in-hand dexterous motions with multifinger robot hands, without sacrificing the passive adaptability in power grasping of standard underactuated hand designs. The spherical hand concept predicts a manipulation workspace with a common center, independent of the object properties or hand configuration. This property was validated through a physical test model that preserved ideal point contacts. Morphological changes in thumb and fingertip design proposed in the spherical hand concept were also applied to a standard three-finger, medium-complexity hand topology used in several commercial offerings [11,12], and it was shown that the precision manipulation workspace was improved.

Maintaining robust and favorable contact conditions remains a considerable challenge. Models typically assume well-defined and deterministic contact constraints. Slip and rolling during manipulation tasks was common despite the implementation of the passive rotary fingertips to maintain point contact constraints. Although these effects were often repeatable and did not always result in a loss of grasp stability, variable contact conditions make planning and control difficult, even when the kinematic topology is designed for a particular motion profile.

Experimental trials utilizing the passive thumb base pivot suggest that reconfiguration in underactuated systems can be leveraged to mitigate undesirable contact conditions. The degree of freedom due to the passive thumb base pivot has not been tested in any prior hand designs, to the authors' knowledge. Furthermore, an optimization of the mechanical design parameters to maximize precision grasp stability was beyond the scope of this study. Additional underactuation may be worth the cost if the reconfiguration is predictable, and contact variance can be minimized.

While there have been many proposed contact models and control schemes for in-hand dexterous manipulation, they typically make the assumption that slip or loss of contact can be either tracked or minimized to a negligible amount through control. This is rarely the case in practical systems, especially those outside of well-structured research environments. This study suggests that underactuated morphologies can make the primary passive system reconfiguration predictable, and consequently minimize the need to track or account for contact behaviors which may be difficult to model, such as rolling and slip. The spherical hand morphologies provide insight into the expected object workspace regardless of the change in contact state, albeit only for the instantaneous motion given the expectation of changing contact conditions. Further future work investigating novel modifications to traditional robotic hand components may reduce the amount of necessary a priori object knowledge required for precision manipulation and make such task primitives more robust to errors accumulated from inconsistent contact conditions.

References

[1] Dai, J. S., Wang, D., and Cui, L., 2009, "Orientation and Workspace Analysis of the Multifingered Metamorphic Hand—Metahand," IEEE Trans. Robot., **25**(4), pp. 942–947.

[2] Higashimori, M., Jeong, H., Ishii, I., Kaneko, M., and Background, A., 2005, "A New Four-Fingered Robot Hand With Dual Turning Mechanism," International Conference on Robotics and Automation (ICRA), Vol. 2, Barcelona, Spain, Apr. 18–22, pp. 2679–2684.

[3] Bicchi, A., and Marigo, A., 2002, "Dexterous Grippers: Putting Nonholonomy to Work for Fine Manipulation," Int. J. Rob. Res., **21**(5–6), pp. 427–442.

[4] Dollar, A. M., and Howe, R. D., 2010, "The Highly Adaptive SDM Hand: Design and Performance Evaluation," Int. J. Rob. Res., **29**(5), pp. 585–597.

[5] Eppner, C., Deimel, R., Álvarez-Ruiz, J., Maertens, M., and Brock, O., 2015, "Exploitation of Environmental Constraints in Human and Robotic Grasping," Int. J. Rob. Res., **34**(7), pp. 1021–1038.

[6] Odhner, L. U., Jentoft, L. P., Claffee, M. R., Corson, N., Tenzer, Y., Ma, R. R., Buehler, M., Kohout, R., Howe, R. D., and Dollar, A. M., 2014, "A Compliant, Underactuated Hand for Robust Manipulation," Int. J. Rob. Res., **33**(5), pp. 736–752.

[7] Hunt, K. H., 1978, *Kinematic Geometry of Mechanisms*, Oxford University Press, New York.

[8] Odhner, L. U., and Dollar, A. M., 2011, "Dexterous Manipulation With Underactuated Elastic Hands," IEEE International Conference on Robotics and Automation, (ICRA), Shanghai, China, May 9–13, pp. 5254–5260.

[9] Rojas, N., and Dollar, A. M., 2014, "Characterization of the Precision Manipulation Capabilities of Robot Hands Via the Continuous Group of Displacements," IEEE/RSJ International Conference on Intelligent Robots and Systems (IROS 2014), Chicago, IL, Sept. 14–18, pp. 1601–1608.

[10] Rojas, N., and Dollar, A. M., 2015, "Gross Motion Analysis of Fingertip-Based Within-Hand Manipulation," IEEE Trans. Robot., **32**(4), pp. 1009–1016.

[11] Ulrich, N. T., Paul, R., and Bajcsy, R., 1988, "A Medium-Complexity Compliant End Effector," IEEE International Conference on Robotics and Automation (ICRA), Philadelphia, PA, Apr. 24–29, pp. 434–436.

[12] Robotiq, 2016, "Robotiq 3-Finger Adaptive Robot Gripper," Robotiq, Lévis, QC, Canada, accessed Oct. 20, 2016, http://www.robotiq.com/en/products/industrial-robot-hand

[13] Bicchi, A., 2000, "Hands for Dexterous Manipulation and Robust Grasping: A Difficult Road Toward Simplicity," IEEE Trans. Robot. Autom., **16**(6), pp. 652–662.

[14] Grebenstein, M., Chalon, M., Friedl, W., Haddadin, S., Wimbock, T., Hirzinger, G., and Siegwart, R., 2012, "The Hand of the DLR Hand Arm System: Designed for Interaction," Int. J. Rob. Res., **31**(13), pp. 1531–1555.

[15] Tischler, C. R., Samuel, A. E., and Hunt, K. H., 1995, "Kinematic Chains for Robot Hands II. Kinematic Constraints, Classification, Connectivity, and Actuation," Mech. Mach. Theory, **30**(8), pp. 1217–1239.

[16] Hervé, J. M., 2004, "Note About the 3-UPU Wrist," Mech. Mach. Theory, **39**(8), pp. 901–904.
[17] Li, Q., Huang, Z., and Hervé, J. M., 2004, "Type Synthesis of 3R2T 5-DOF Parallel Mechanisms Using the Lie Group of Displacements," Trans. Robot. Autom., **20**(2), pp. 173–180.
[18] Ma, R. R., Rojas, N., and Dollar, A. M., 2015, "Towards Predictable Precision Manipulation of Unknown Objects With Underactuated Fingers," 3rd ASME/IFToMM International Conference on Reconfigurable Mechanisms and Robots (ReMAR 2015), Beijing, China, July 20–22, pp. 927–937.
[19] Odhner, L. U., Ma, R. R., and Dollar, A. M., 2014, "Exploring Dexterous Manipulation Workspaces With the iHY Hand," J. Robot. Soc. Jpn., **32**(4), pp. 318–322.
[20] Ma, R. R., Odhner, L. U., and Dollar, A. M., 2015, "Yale OpenHand - Model O," The Grab Lab, Yale University, New Haven, CT, accessed Oct. 20, 2016, http://www.eng.yale.edu/grablab/openhand/model_o.html
[21] Bullock, I. M., Feix, T., and Dollar, A. M., 2014, "Dexterous Workspace of Human Two-and-Three-Fingered Precision Manipulation," IEEE Haptics Symposium (HAPTICS), Houston, TX, Feb. 23–26, pp. 41–47.
[22] ATC, 2016, "trakSTAR/driveBAY," Ascension Technology Corp., Shelburne, VT, accessed Oct. 20, 2016, http://www.ascension-tech.com/products/trakstar-drivebay/
[23] Rusu, R. B., and Cousins, S., 2011, "3D is Here: Point Cloud Library (PCL)," IEEE International Conference on Robotics and Automation, (ICRA), Shanghai, China, May 9–13, pp. 1–4.
[24] Akkiraju, N., Edelsbrunner, H., Facello, M., Fu, P., Mucke, E. P., and Varela, C., 1995, "Alpha Shapes: Definition and Software," First International Computational Geometry Software Workshop, Minneapolis, MN, Jan. 20.
[25] Gamage, S. S. H. U., and Lasenby, J., 2002, "New Least Squares Solutions for Estimating the Average Centre of Rotation and the Axis of Rotation," J. Biomech., **35**(1), pp. 87–93.
[26] Chang, D. C., and Cutkosky, M. R., 1995, "Rolling With Deformable Fingertips," IEEE/RSJ International Conference on Intelligent Robots and Systems, Pittsburgh, PA, Aug. 5–9, pp. 194–199.
[27] Thuc, P., Nguyen, A., and Arimoto, S., 2002, "Dexterous Manipulation of an Object by Means of Multi-DOF Robotic Fingers With Soft Tips," J. Robot. Syst., **19**(7), pp. 349–362.
[28] Odhner, L. U., and Dollar, A. M., 2015, "Stable, Open-Loop Precision Manipulation With Underactuated Hands," Int. J. Rob. Res., **34**(11), pp. 1347–1360.
[29] Borràs, J., and Dollar, A. M., "Dimensional Synthesis of a Three-Fingered Dexterous Hand for Maximal Manipulation Workspace," Int. J. Rob. Res., **34**(14), pp. 1731–1746.
[30] Howard, W. S., and Kumar, V., 1996, "On the Stability of Grasped Objects," IEEE Trans. Robot. Autom., **12**(6), pp. 904–917.
[31] Odhner, L. U., Ma, R. R., and Dollar, A. M., 2013, "Experiments in Underactuated In-Hand Manipulation," Exp. Robot., **88**, pp. 27–40.
[32] Balasubramanian, R., Belter, J. T., and Dollar, A. M., 2012, "Disturbance Response of Two-Link Underactuated Serial-Link Chains," ASME J. Mech. Rob., **4**(2), p. 021013.
[33] Yoshikawa, T., 1999, "Passive and Active Closures by Constraining Mechanisms," ASME J. Dyn. Syst. Meas. Control, **121**(3), pp. 418–424.
[34] Hanafusa, H., and Asada, H., 1977, "Stable Prehension of Objects by the Robot Hand With Elastic Fingers," Trans. Soc. Instrum. Control Eng., **13**(4), pp. 370–377.
[35] Maeda, Y., Kodera, N., Egawa, T., and Definition, A., 2012, "Caging-Based Grasping by a Robot Hand With Rigid and Soft Parts," IEEE International Conference on Robotics and Automation (ICRA), St. Paul, MN, May 14–18, pp. 5150–5155.
[36] Smooth-On, 2016, "VytaFlex® Urethane Rubber," Smooth-On, Inc., Macungie, PA, accessed Oct. 20, 2016, http://www.smooth-on.com/Urethane-Rubber-an/c6_1117_1142/index.html